Published in final edited form as:
Nat Cell Biol. 2015 April ; 17(4): 409–420. doi:10.1038/ncb3135.

Control of cell-cell forces and collective cell dynamics by the intercellular adhesome

Elsa Bazellières[1], **Vito Conte**[1], **Alberto Elosegui-Artola**[1], **Xavier Serra-Picamal**[1], **María Bintanel-Morcillo**[1], **Pere Roca-Cusachs**[1,2], **José J Muñoz**[3], **Marta Sales-Pardo**[4], **Roger Guimerà**[4,5], and **Xavier Trepat**[1,2,5,*]

[1]Institute for Bioengineering of Catalonia, Barcelona, Spain.

[2]Unitat de Biofísica i Bioenginyeria, Facultat de Medicina, Universitat de Barcelona, and CIBERES, Spain

[3]Laboratori de Càlcul Numèric, Department of Applied Mathematics III, Universitat Politècnica de Catalunya, Barcelona, Spain.

[4]Departament d'Enginyeria Química, Universitat Rovira i Virgili, Tarragona 43007, Catalonia, Spain

[5]Institució Catalana de Recerca i Estudis Avançats (ICREA), Barcelona, Spain.

Abstract

Dynamics of epithelial tissues determines key processes in development, tissue healing, and cancer invasion. These processes are critically influenced by cell-cell adhesion forces. However, the identity of the proteins that resist and transmit forces at cell-cell junctions remains unclear, and how these proteins control tissue dynamics is largely unknown. Here we provide a systematic study of the interplay between cell-cell adhesion proteins, intercellular forces, and epithelial tissue dynamics. We show that collective cellular responses to selective perturbations of the intercellular adhesome conform to three mechanical phenotypes. These phenotypes are controlled by different molecular modules and characterized by distinct relationships between cellular kinematics and intercellular forces. We show that these forces and their rates can be predicted by the concentrations of cadherins and catenins. Unexpectedly, we identified different mechanical roles for P-cadherin and E-cadherin; while P-cadherin predicts levels of intercellular force, E-cadherin predicts the rate at which intercellular force builds up.

*Corresponding author: Prof. Xavier Trepat, Institute for Bioengineering of Catalonia C/ Baldiri Reixac 15-21 Barcelona 08028 Spain. Tel: +34934020265 xtrepat@ub.edu.

Author contributions

E.B and X.T conceived the study and designed experiments. E.B., M.B., and A.E performed experiments. E.B, V.C, and A.E analyzed data. X.S and P.R developed data analysis tools. V.C. and J.J.M. developed computational mechanics tools. M.S and R.G performed unsupervised clustering analysis and LOOCV analysis. E.B., M.S, R.G, and X.T. wrote the manuscript. All authors discussed and interpreted results and commented on the manuscript.

Europe PMC Funders Author Manuscripts

Introduction

The homeostasis of epithelial tissues and its disruption during disease are enabled by collective cellular processes such as growth, migration, and remodeling[1-3]. Each of these collective processes has long been known to be critically influenced by cell-cell adhesion complexes. To a significant extent, this critical influence has its mechanistic origin in the ability of cell-cell adhesions to transmit physical forces[4-13].

Force transmission through intercellular junctions is traditionally attributed to adherens junctions, which provide a physical connection between the actomyosin cytoskeleton and transmembrane proteins of the cadherin superfamily[14-17]. However, the identity of the molecules that transmit physical forces in adherens junctions remains controversial. For example, epithelial cells often express several cadherin isoforms[18, 19], including E-cadherin, N-cadherin, and P-cadherin[18,19]. The balance in the expression of these different cadherins is known to be essential to maintain tissue homeostasis[18, 20-22] but the extent to which each classical cadherin is involved in force transmission is unknown[18-23]. Moreover, the network of proteins that provides a physical connection between cadherins and the cytoskeleton is also incomplete. β-catenin and α-catenin link cadherins and F-actin[24] but other proteins such as ZO-1, vinculin, and lima have also been proposed to contribute to force transmission[17, 25, 26].

Besides adherens junctions, the actomyosin cytoskeleton of adjacent cells is also connected through tight junctions, which comprise transmembrane receptors such as claudins, occludin, and JAM-A, as well as intracellular linkers such as ZO-1, ZO-2, and ZO-3[27]. Tight junctions are typically associated with epithelial sealing rather than force transmission, but no experimental evidence has so far ruled out the ability of tight junctions to resist and transmit physical forces. In addition to the actin cytoskeleton, forces within epithelial sheets have also been proposed to be transmitted by intermediate filaments within cells and by desmosomes between cells[28-30]. Finally, gap junctions, which play a major role in controlling the intercellular transit of ions and small solutes between cells, have been shown to be mechanosensitive[31], thus raising the possibility that they might play a mechanical role in epithelial tissue dynamics.

Here we used micropatterned sheets of epithelial cells as a model system to study the interplay between intercellular adhesion proteins, physical forces, and tissue dynamics. We designed a minimal custom library of validated siRNAs targeting the main molecular components of the intercellular adhesome. For each siRNA perturbation we measured cellular velocities and deformation rates, as well as inter-, intra-, and extra-cellular forces. Using unsupervised clustering analysis, we identified systematic relationships between these physical properties and molecular control modules within the adhesome. Using a cross-validation analysis we established the ability of intercellular adhesion proteins to quantitatively predict tissue dynamics.

Results

Intercellular cohesiveness increases with monolayer expansion

We developed an assay to measure in parallel the epithelial dynamics of multiple expanding monolayers (Fig. 1a,b). Using soft lithography, thin polydimethylsiloxane (PDMS) membranes with a rectangular opening were fabricated and deposited on top of a collagen I-coated polyacrylamide gel substrate[13, 32]. We then seeded normal breast epithelial cells (MCF10A) and allowed them to adhere and spread until they formed a confluent monolayer. After 5 hours of culture, F-actin was largely cortical but the monolayer was not cohesive; cadherins, catenins, and ZO-1 were either fully cytoplasmic or weakly localized at the lateral cell-cell contact areas (Fig. 1c,e).

Upon lifting the PDMS membrane, the monolayer expanded toward the available gel surface and, after 8 hours of migration, its area had increased by ~30% (Fig. 2a,b,i, Supplementary Video 1). At this point, cadherins, catenins, and ZO-1 progressively accumulated at the cell cortex, and this accumulation was more pronounced in the central region of the monolayer (Fig. 1d,f). Thus, as the monolayer expanded it increased its structural cohesiveness through recruitment of cell-cell adhesion proteins to the cell cortex.

As the monolayer increases its cohesiveness, cell migration slows down and intercellular forces buildup

We next studied how the increase in monolayer cohesiveness was paralleled by changes in physical properties of the constituent cells, including cellular velocities, inter- and intra-cellular forces, and traction forces at the cell-substrate interface. To map cell velocities during monolayer expansion we used particle imaging velocimetry (PIV)[13]. Velocity fields showed large spatial heterogeneities that spanned several cell diameters (Fig. 2c,d, Supplementary Video 2)[6, 13]. Despite these large fluctuations, cells moved predominantly away from the initial pattern and, as the monolayer expanded, the average cell velocity decreased (Fig. 2 j).

Simultaneously with cell velocities we measured traction forces exerted by cells on the underlying substrate. From the onset of monolayer expansion, traction forces exhibited a punctate spatial distribution characterized by rapid fluctuations in magnitude and direction (Fig. 2e,f, Supplementary Video 2). To assess the total traction exerted by cells in the monolayer we computed the strain energy density (U) transferred by cells to the gel. U increased with time and tended to saturate after 300 minutes (Fig. 2k), indicating that cells approached a mechanical steady state.

We next asked whether the accumulation of adhesion proteins at intercellular contacts was paralleled by an increase in cell-cell forces. To address this question we used Monolayer Stress Microscopy (MSM), which computes the state of mechanical stress (force per unit cross-sectional area) everywhere within the cell sheet [6, 13, 33-35]. MSM is based on the principle that traction forces applied at the cell-gel interface must be balanced by intra- and intercellular forces [36-39]. For simplicity, we mainly focused on σ_{xx}, the stress component in the direction of expansion of the monolayer, and referred to it indistinctly as monolayer tension or intercellular tension (see Supplementary Note for other stress components).

Monolayer tension displayed well-known features of expanding epithelial sheets including dynamic heterogeneities and supracellular fluctuations (Fig. 2g,h, Supplementary Video 2)[6, 13, 33]. Similarly to the case of traction forces, all components of the stress tensor increased monotonically with time and tended to plateau as expansion slowed down (Fig. 2l).

Taken together, our data put forward the following scenario. As the monolayer expands, it matures its intercellular adhesions with a cortical recruitment of cadherins, catenins, and ZO-1. These structural changes are paralleled by a progressive decrease in cell velocity, and a pronounced increase in cell-substrate forces and intercellular tension.

Downregulation of cell-cell adhesion proteins alters cell velocities, cell tractions, and intercellular tension

We next sought to identify what proteins are involved in the regulation and transmission of monolayer tension. To do so, we designed a minimal siRNA library to selectively knock down the main molecular players of the intercellular adhesome (Supplementary Fig. 1a). Specifically, we targeted key transmembrane proteins associated with adherens junctions, tight junctions, desmosomes, and gap junctions. In addition, we targeted a subset of cytoplasmic proteins that have been shown or proposed to be involved in linking these transmembrane proteins to the actin and intermediate filament cytoskeleton.

To effectively knock down genes coding for intercellular adhesion proteins we transfected cells with a pool of 3 distinct siRNAs and carried out monolayer expansion experiments 5 days later. All siRNA pools efficiently down-regulated their respective target genes with an average mRNA knockdown of 81% ± 11% (mean ± SEM) (Supplementary Fig. 1b).

Representative maps of v_x, T_x and σ_{xx} for a subset of siRNAs are shown in Figs. 3 and 4 (see also Supplementary Figs. 2 to 7 for a complete set of representative experiments). These maps confirm previous studies showing that down-regulation of E-cadherin or N-cadherin has no impact on cellular velocities (Fig. 3b, Supplementary Fig. 2)[21, 40]. Our data show, further, that loss of function of these cadherins does not influence the transmission of intercellular tension (Fig. 3b, Supplementary Fig. 2, Supplementary Video 3). By contrast, knocking down P-cadherin led to monolayer dissociation, an increase in cell velocity and a sharp drop in monolayer tension (Fig. 3c). Similarly, down-regulation of catenins led to faster monolayer expansion and lower intercellular tension (Fig. 3d-f, Supplementary Fig. 3). Knockdown of lima1 and Drr1 did not impact significantly monolayer dynamics (Supplementary Fig. 4). Together, these data suggest that P-cadherin associates with catenins to mediate intercellular force transmission in MCF10A cells.

siRNAs targeting desmosomes, tight junctions, and gap junctions also altered cellular velocities, tractions, and tensions (Fig. 4a-f, Supplementary Figs. 5-7). Downregulation of tight junction proteins ZO-1 and ZO-3 led to marked but opposite changes in monolayer mechanics (Fig. 4c,d). Downregulation of desmosomal proteins caused minor changes in monolayer forces and kinematics with the exception of Dsc3, which slowed down cell migration (Fig. 4e, Supplementary Fig. 7). Finally, siRNAs targeting gap junction protein Cx43 caused a weak decrease in traction forces and intercellular tension (Fig. 4f). Thus,

proteins associated with junctional complexes other than adherens junctions also appear to be involved in the regulation of monolayer dynamics.

We next focused on the time evolution of monolayer dynamics in response to siRNAs. For each time point, we averaged maps of each physical property across space and over all experimental repeats (see Methods and Supplementary Note). The time evolution of these averages showed that the global trends of control experiments were generally conserved under siRNA perturbations but with clear exceptions (Fig. 3g-j, Fig. 4g-j, Supplementary Fig. 8). For example, the general tendency of intercellular forces to increase with monolayer expansion was disrupted by a number siRNAs -e.g. sip120, siβcat, and siPcad (Fig. 3j). Taken together, our data indicate that proteins from distinct junctional complexes alter monolayer kinematics and forces, as well as the time evolution of these physical properties.

Forces and kinematics are anti-correlated

The diversity of responses to siRNAs prompted us to study systematically the mechanical phenotypes explored by cell monolayers. To do so, we first asked whether physical properties that define tissue dynamics are linked through universal relationships or whether they are generally uncorrelated. We began by identifying a minimal set of properties that fully captured the diversity of observed mechanical phenotypes (Supplementary Note). We selected the following properties, averaged over time, space, and experimental repeats: cell velocity V_x, cell deformation rate $\dot{\varepsilon}_{xx}$, increase in monolayer area ΔA, strain energy density transferred by cells to the substrate U, and maximum shear stress σ_s. In addition, to capture monolayer tension to first order in time we considered the average value of σ_{xx} at the end of the experiment $\left(\sigma_{xx}^{f}\right)$ and the average slope of its time evolution $(\dot{\sigma}_{xx})$. In this way, we were able to summarize our data in a $m \times n$ matrix comprising m siRNA perturbations, and n physical properties (m=21, n=7). From this data matrix, we computed a matrix Z, in which each element Z_{ij} (element located on row i and column j) contains the z-score of the physical property j in response to a siRNA perturbation i (Fig. 5a) (see Methods for a description of z-score calculations).

We then computed a cross-correlation between z-scores of each possible pair of physical variables (i.e., correlations between columns in Fig. 5a). Among the m siRNA perturbations, we considered only the subset of q perturbations having at least one physical property that differed from the control by more than two standard deviations (q=12). Correlation analysis yielded a $n \times n$ symmetric matrix Cp, where each element Cp_{ij} indicates the correlation between physical properties i and j (Fig. 5b). We then used an unsupervised algorithm[41] to cluster together the physical properties with highest correlation (Supplementary Note).

Our analysis unveiled two clusters of highly correlated physical properties (Fig. 5b). The first cluster comprises physical properties that describe monolayer kinematics, namely, velocity, increase in monolayer area, and deformation rate. The second cluster comprises physical variables that describe monolayer forces, namely, the strain energy density, the maximum shear stress, monolayer tension at the end of the experiment and the buildup rate of monolayer tension.

siRNA perturbations can be sorted according to their impact on physical properties

We next asked what siRNA perturbations had a similar impact on physical properties. To address this question, we computed correlations between pairs of siRNA perturbations (i.e. correlations between rows in Fig. 5a). The resulting correlation matrix is a $q \times q$ symmetric matrix Cs, where each element Cs_{ij} indicates the correlation between siRNA perturbations i and j (Fig. 5c).

Our unsupervised algorithm identified three clusters of siRNAs as regards their impact on physical properties (Fig. 5c). The first cluster includes only the siRNAs targeting ZO-1, which showed a correlation profile that was clearly distinct from any other siRNA perturbation. The second cluster comprises siRNAs targeting all adherens junction proteins as well as tight junction protein occludin. The third cluster includes siRNAs targeting proteins from diverse intercellular complexes including tight junction proteins Cldn8, ZO-3 and JAM-A, gap junction protein Cx43, and desmosomal protein Dsc3.

Cell monolayers explore distinct mechanical phenotypes

We next used the unsupervised clustering analysis of physical properties (Fig. 5b) and siRNA perturbations (Fig. 5c) to re-organize the original data matrix (Fig. 5a) into distinct mechanical phenotypes (Fig. 5d). The result is a $q \times n$ matrix in which siRNAs (rows) and physical properties (columns) are ordered according to the results from the cross-correlation and unsupervised clustering algorithms. This analysis identified three distinct mechanical phenotypes. The most common phenotype, which we call Fast/Weak (FW) phenotype, was characterized by an increase in physical properties associated with kinematics and a decrease in physical properties associated with forces. This phenotype was expressed when proteins from adherens junctions were knocked down. The second phenotype was also characterized by a decrease in physical forces, but in this case kinematics remained largely unchanged. We call this phenotype Steady/Weak (SW). It was observed during loss of function of gap junction protein Cx43, tight junction proteins Cldn8, ZO-3, and JAM-A, and desmosomal protein Dsc3. The third phenotype was a Fast/Strong (FS) phenotype in which cells migrated and deformed rapidly while exerting strong cell-cell and cell-substrate forces. This phenotype was rare, being observable only in response to siRNA against ZO-1. It is consistent with the recent discoveries that ZO-1 depletion increases contractility of perijunctional acto-myosin[42] and that ZO-1 binds integrins in lamellipodia[43].

The intercellular adhesome is a highly co-regulated system

Our analysis thus far allowed us to associate specific siRNAs with specific mechanical phenotypes. This association is not necessarily mechanistic at the molecular level, however, because down-regulation of one specific protein may lead to changes in physical properties indirectly through the action of other co-regulated proteins. To address co-regulation we selected a subset of siRNA perturbations from our library and measured the effect of these perturbations on the concentrations of cell-cell adhesion proteins. For each siRNA perturbation, we used quantitative Western Blot to measure total protein concentrations relative to control experiments for E-, N-, P-cadherin, β-catenin, α-catenin, p120, ZO-1, and occludin (see Supplementary Note for a co-regulation analysis of gap junction, tight junction, and desmosome hits).

Measurements of protein concentrations showed that each targeted protein was effectively down-regulated with an average knock-down efficiency of 86.3% ± 14.5% (mean+SEM) (Supplementary Fig. 1c). As expected in a highly co-regulated system[21,35], each siRNA altered not only the concentrations of the targeted proteins but also the concentrations of non-targeted proteins. For example, siRNAs against p120 caused a substantial decrease in the concentrations of all cadherins and catenins (Fig. 6a). To study co-regulation patterns systematically we computed the correlation between pairs of proteins by calculating the cosine similarity between the vectors of z-scores of protein concentrations (columns in Fig. 6a). We then ordered the resulting $k \times k$ correlation matrix ($k=8$ proteins) using the unsupervised clustering algorithm (Fig. 6b). All proteins associated with adherens junctions, with the exception of N-cadherin, showed correlations that were highly variable but exclusively positive. These findings show that cadherins and catenins considered in this study are generally not involved in compensatory feedback loops in which a decrease in expression of one protein would be systematically compensated by an increase in expression of another one. Instead, expression levels of different adherens junction proteins in response to siRNA perturbations varied in parallel. N-cadherin and occludin were the exception to this rule and showed expression patterns that were either uncorrelated or anticorrelated with those of other adherens junction proteins (Fig. 6b).

P-cadherin predicts the magnitude of intercellular tension, while E-cadherin predicts of its buildup rate

We next asked whether protein concentrations might be predictive of the physical properties that characterize epithelial dynamics. As the simplest possible predictive model we considered a linear relationship between any physical property X_j and any protein concentration $[p_i]$:

$$X_j = A + B\,[p_i] \quad \text{Eq.1}$$

where A and B are constant coefficients for each pair protein/physical property (see Supplementary Note for linear models involving multiple protein concentrations).

To assess the predictive power of this model we performed a leave-one-out cross-validation (LOOCV) analysis (Methods). LOOCV analysis revealed that simple linear models involving only one protein were generally poor predictors of physical properties. None of the protein concentrations was able to predict kinematic properties such as monolayer expansion, cellular velocity, or deformation rates. Protein concentrations were also unable to predict the magnitude of traction forces. By contrast, concentrations of E- and P-cadherin were significant predictors of intercellular tension and its time evolution. P-cadherin -but not E-cadherin- was a significant predictor of the average intercellular tension σ_{xx}^{m} (Fig. 6c, Supplementary Table 2) as well as of intercellular tension at the end of the experiment σ_{xx}^{f} (Fig. 6d, Supplementary Table 2). By contrast, E-cadherin -but not P-cadherin- was a significant predictor of the rate at which intercellular tension builds up (Fig. 6e, Supplementary Table 2). Surprisingly, these findings suggest that P-cadherin and E-cadherin play fundamentally distinct roles in controlling force transmission at intercellular junctions.

Specifically, they suggest that P-cadherin is involved in the control of equilibrium values of intercellular tension, while E-cadherin is involved in the control of the rate at which intercellular tension varies over time.

P-cadherin and E-cadherin show distinct responses to mechanical stress

How do two proteins with high homology play such fundamentally different roles in the regulation of intercellular tension? An appealing possibility is that mechanical tension triggers distinct feedback loops depending on whether it is applied through P-cadherin or E-cadherin. To test this possibility we coated magnetic beads with either P- or E-cadherin and allowed them to bind to cadherin receptors at the apical surface of an MCF10A monolayer. We then used magnetic tweezers to subject the cell-bead junction to a pattern of oscillatory pulling forces (Fig. 7a)[23, 44, 45]. By tracking bead trajectories during force application we studied the mechanical response of the cell to forces exerted through P- or E-cadherin receptors. Pulling on beads coated with E-cadherin led to a pattern of oscillatory bead displacements whose amplitude decreased with time (Fig. 7b,c). This type of cellular response to force has been extensively studied using beads coated with either extracellular matrix proteins[46, 47] or cadherins[23, 45]; it indicates that tension triggers internal feedback loops that allow the cell to actively adapt to the extracellular force by reinforcing its structural connection with the bead. By contrast, pulling on beads coated with P-cadherin led to a pattern of oscillatory displacements of constant amplitude (Fig. 7b,c), thus indicating that P-cadherin junctions do not reinforce.

Application of pulling forces of varying amplitude revealed a weak tendency of reinforcement through E-cadherin to increase with applied force, and confirmed the absence of reinforcement through P-cadherin (Fig. 7d,e). Decreasing the concentration of P-cadherin at the bead surface changed the initial stiffness of the cell-bead contact but not its time evolution (Fig. 7f-h). By contrast, decreasing the concentration of E-cadherin resulted in no changes in the initial stiffness but in a significant decrease in the stiffening rate (Supplementary Fig. 7f-h). These experiments confirm our predictive models by showing that P-cadherin and E-cadherin play distinct control roles by activating distinct feedback loops downstream of intercellular tension.

In the absence of E-cadherin, P-cadherin triggers mechanotransduction

In the specific case of E-cadherin depletion, our measurements of mechanotransduction using magnetic tweezers (Fig. 7b,c) and the results of our predictive models (Fig. 6e) would seem to be in contradiction with our measurements of monolayer tension using MSM (Fig. 3b). Indeed, magnetic tweezers experiments and predictive models reveal a key role for E-cadherin in the dynamic regulation of monolayer tension (Fig. 7 and Fig. 6e), whereas knocking down E-cadherin did not alter monolayer tension and cohesion (Fig. 3b, Fig 7i,j). This apparent contradiction could originate from a functional redundancy between E-cadherin and P-cadherin. To explore this possibility we used magnetic tweezers to pull on beads coated with P-cadherin attached to cells depleted of E-cadherin. Under such conditions, and contrary to the case of control cells, pulling on P-cadherin caused reinforcement of the cell-bead contact (Fig. 7b,c). Thus P-cadherin is able to trigger mechanotransduction feedback loops, but it does so only in the absence of E-cadherin. Such

functional redundancy reconciles the apparent conflict between our distinct measurement techniques and analysis strategies; when E-cadherin is knocked down, P-cadherin is able to take over its role as a tension regulator, thereby preventing a decrease in intercellular tension.

Vinculin is involved in mechanotransduction through P-cadherin and E-cadherin

Our previous experiments raise the possibility that mechanotransduction through P- and E-cadherin is mediated by the same molecular pathway but that E-cadherin has higher affinity than P-cadherin for that pathway. An appealing molecular candidate to be involved in such common pathway is vinculin, which binds to a cryptic site of α-catenin to trigger mechanotransduction[48, 49]. To test this possibility we first measured the localization of vinculin after force application. After pulling on E-cadherin in control cells we observed an accumulation of vinculin at the cell-bead contact (Fig. 8a,d), in agreement with previous findings[45, 50]. This accumulation was significantly higher than that observed after pulling on P-cadherin in control cells (Fig. 8b,d). However, after pulling on P-cadherin in cells depleted of E-cadherin, the levels of vinculin accumulation at the cell-bead contact were similar to those observed in beads coated with E-cadherin in control cells (Fig. 8c,d). These experiments show that vinculin accumulation at the cell-bead contacts parallels mechanotransduction responses.

To further support the involvement of vinculin in mechanotransduction through both E- and P-cadherin we hypothesized that vinculin knockdown should impair E-cadherin and P-cadherin reinforcement. Consistent with this hypothesis, pulling on magnetic beads coated with E-cadherin in cells depleted of vinculin resulted in weaker reinforcement (Fig 8e). Similarly, pulling on magnetic beads coated with P-cadherin in cells depleted of both E-cadherin and vinculin also led to weaker reinforcement (Fig 8e). Together, these experiments support that P- and E-cadherin compete for a common mechanotransduction pathway involving vinculin.

Discussion

Epithelial dynamics is traditionally interpreted in the context of a smooth or abrupt transition between epithelial and mesenchymal states; as the concentrations of intercellular adhesion proteins decrease, cells within tissues lose cohesiveness and speed up migration[51, 52]. Here we showed that the phenotypic plasticity of monolayer dynamics is much richer than previously thought; by expressing distinct combinations of cell-cell adhesion proteins, cells control their velocity and intercellular tension independently.

Recently, experiments using nearly identical approaches have led to conflicting conclusions as regards the correlation between intercellular force and the localization of E-cadherin at cell-cell junctions[37-39]. Our findings suggest that this discrepancy might be explained by different confounding factors. Firstly, E-cadherin should not be regarded as the only cadherin involved in the regulation of intercellular tension; other cadherins, such as P-cadherin, should be taken into account to understand force balance at intercellular junctions. Secondly, different cadherins can exhibit mechanical redundancy when expressed in isolation but trigger different mechanotransduction feedback loops when expressed in

conjunction. Finally, the total protein concentration, and not necessarily the amount of protein that localizes at intercellular junctions, is a robust determinant of intercellular tension. Once these considerations are taken into account, our study shows that simple models can predict monolayer tension and its buildup rate. Given the high connectivity of cell-cell adhesion proteins (E-cadherin has 96 known binding partners and β-catenin has 243 [53]) the existence of such simple models is remarkable.

When E-cadherin was knocked down, the rate of stress buildup of the cell monolayer remained unaltered. This result was not well captured by our predictive model based solely on E-cadherin concentration (see leftmost data point in Fig. 6e). Using magnetocytometry, we showed that this discrepancy originates from a functional redundancy between P- and E-cadherin (Fig. 7). Interestingly, this redundancy appeared to be active only at relatively low concentrations of E-cadherin, suggesting that E-cadherin has a much higher affinity than P-cadherin for the mechanotransduction machinery of the cell. In this connection, it is worth emphasizing that models involving concentrations of multiple proteins produced much more accurate predictions that one-protein models.

P- and E-cadherin have highly homologous sequences but are attributed markedly different roles in physiology and cancer. They are usually co-expressed in the basal layer of stratified epithelia, where proliferation, differentiation, and compartmentalization take place[54, 55]. By contrast only E-cadherin is usually expressed in suprabasal differentiated layers where mechanical function is less diverse. In cancer, E-cadherin expression is generally associated with positive prognosis, whereas P-cadherin expression is associated with increased cancer cell migration and invasion[54, 55]. Interestingly, in cancers where only P- or E- cadherin are expressed, both proteins act as suppressors of cancer invasion[56-59]. Such behavior is consistent with our findings that P-cadherin and E-cadherin play a similar mechanical role when one of them is expressed dominantly. By contrast, aggressive invasion is observed when P- and E- cadherin are jointly expressed[22]. Further studies should address whether underlying mechanisms involve the competition of cadherins for a joint mechanotransduction pathway as reported in our study.

The simultaneous expression of two distinct proteins, one proportional to the magnitude of a physical quantity and one proportional to the time derivative of this quantity, provides the cell with advanced control capabilities. In proportional control systems, which are the simplest control systems involving feedback loops, the control signal is proportional to the difference between the value of the output and its desired setpoint[60]. Control theory shows that the efficiency of this control strategy is significantly improved if the control signal also takes into account the time derivative of the output, or in other words, how fast the desired setpoint is being reached[60, 61]. Derivative control action of this kind is widely used in engineering to compensate rapid changes in the output and to reduce instabilities. Here we showed that the concentrations of P- and E-cadherin are good predictors of intercellular tension and its time derivative, respectively. These findings raise the possibility that adherens junctions act as proportional-derivative feedback systems to control intercellular tension.

METHODS

MCF10A cell culture

MCF10A cells were grown on DMEM-F12 media supplemented with 5% Horse Serum, 100U/mL Penicillin, 100μg/mL Streptomycin, 20ng/mL EGF, 0.5mg/mL Hydrocortisone, 100 ng/mL Cholera Toxin, and 10 ug/mL Insulin.

Polyacrylamide gel substrates

Polyacrylamide gels with a Young's modulus of 12 kPa were prepared as described previously[13, 62, 63]. Briefly, a solution containing 19% acrylamide, 8% bis-acrylamide, 0.5% ammonium persulfate, 0.05% tetramethylethylenediamine, 0.64% of 200-nm-diameter red fluorescent carboxylate-modified beads and 2mg/mL NH-acrylate was prepared and allowed to polymerize. After polymerization, gels were incubated with 0.1 mg/mL of collagen I overnight.

PDMS membranes

Polydimethylsiloxane (PDMS) membranes were fabricated according to procedures described previously[13, 32, 64]. Briefly, SU8-50 masters containing rectangles of 300×2,500 μm were raised using conventional photolithography. Uncured PDMS was spin-coated on the masters to a thickness lower than the height of the SU8 feature (35 μm) and cured for 2hr at 60°C. A thick border of PDMS was left at the edges of the membranes for handling purposes. PDMS was then peeled off from the master and kept in ethanol at 4°C until use.

Monolayer patterning

To pattern the cells on top of the polyacrylamide gels, a PDMS membrane was deposited on top of the polyacrylamide gel and 20,000 cells were seeded within the rectangle defined by the PDMS stencil. Cells were allowed to adhere and proliferate on the gel for 5 hours. 40 minutes before time lapse analysis, the PDMS membrane was carefully removed allowing the cells to migrate toward the freely available substrate.

siRNAs transfection

siRNA reverse transfections were performed by mixing Lipofectamine RNAiMAX Reagent with 100 pmoles of a pool of 3 siRNAs and 450,000 freshly trypsinized MCF10A cells (see Supplementary Table 4 for siRNA sequences). Cells were then seeded on 6-well plates. 5 days after transfection cells were trypsinized and seeded on soft polyacrylamide gels. ~90% of the cells were successfully transfected as measured using Block-it Alexa Fluor Red Fluorescent Oligo.

RT-PCR

RT-PCR experiments were performed according to the manufacturer's instructions (Applied Biosystems). Total mRNA was extracted from MCF10A control and knockdown cells using the PARIS kit. RNA samples were reverse-transcribed into cDNA using the High Capacity RNA-to-cDNA master mix. Taqman Gene Expression Assays were used to detect endogeneous mRNA levels. The housekeeping gene rps18 was used as an endogeneous

control for normalization (see Supplementary Table 4 for Taqman probe list). PCR was performed on a 7500 Fast Real Time PCR System (Applied Biosystems).

Protein quantification

Protein expression levels were measured using Western Blot. Cells were lysed for protein extraction using lysis buffer (Tris 20mM pH8, NaCl 150 mM, EDTA 1mM, EGTA 1mM, 1% Triton-X100, antipaine 1μg/mL, pepstatine 1μg/mL, benzamidine 15μg/mL, leupeptine 1μg/mL, orthovanadate 0.1mM). Cell lysates were then mixed with Laemli 1X and heated at 95°C for 5 minutes. Next, cell lysates were loaded to 4-20% polyacrylamide gels (Bio-Rad) for electrophoresis. Proteins were then transferred to a nitrocellulose membrane (Whatman, GE Healthcare Life Sciences), which was blocked with 5% dry-milk-Tris Buffer saline-0.2% Tween, and incubated with primary antibodies (overnight at 4°C) followed by the horseradish peroxidase coupled secondary antibodies (1h, room temperature). Bands were revealed using the LumiLight kit (Roche) and the intensity of the bands was quantified using ImageJ software. Tubulin was used as an endogeneous control for normalization. Protein concentrations are reported relative to the control.

Immunostaining

MCF10A cells were washed with PBS, fixed with 3% paraformaldehyde for 10 minutes and permeabilized in 0.1% triton X-100 for 5 minutes. Cells were blocked in 10% FBS for 1 hour before being incubated for 4 hours with primary antibodies. After incubation with the appropriate fluorescence-conjugated secondary antibodies, cells were washed and mounted in Mowiol reagent. Images were acquired with a Nikon C1Si confocal microscope, using a 60× 1.4NA lens.

Antibodies

The primary antibodies used were: anti-Ecadherin monoclonal antibody (clone 36, BD Transduction Laboratories, n° 610181), anti-Ncadherin monoclonal antibody (clone 8C11, Thermo Scientific, n° MA1-2002), anti-Pcadherin monoclonal antibody (clone 6A9, Upstate MerckMillipore, n° 05-916), anti-βcatenin monoclonal antibody (clone 14, BD Transduction Laboratories, n° 610153), anti-αcatenin monoclonal antibody (clone 15D9, Enzo Life Sciences, n° ALX-804-101-C100), anti-p120 catenin monoclonal antibody (clone 98, BD Transduction Laboratories, n°610133), anti-Occludin monoclonal antibody (clone OC-3F10, Invitrogen, n° 33-1500), anti-ZO1 rabbit polyclonal antibody (Invitrogen, n°61-7300), anti-αTubulin monoclonal antibody (clone B-5-1-2, Sigma-Aldrich, n° T5168), anti-Vinculin monoclonal antibody (clone 7F9, EMD Millipore, n° MAB6574), anti-Desmocollin3 rabbit polyclonal antibody (ABGENT, n° AP16771b) , anti-JamA monoclonal antibody (clone EP1042Y, EMD Millipore, n°04-593), anti-Connexin43 rabbit polyclonal antibody (EMD Millipore, n° AB1728), anti-ZO3 monoclonal antibody (clone D57G7, Cell Signaling, n° 3704). For western blotting, all the antibodies were diluted 1/500, except –αTubulin 1/10000. For immunofluorescence, all the antibodies were diluted 1/200. The secondary antibodies used for western blots were: peroxidase-conjugated anti-mouse IgG (Jackson Immuno Research, n° 715-035-151) and peroxidase-conjugated anti-rabbit IgG (Merck Millipore, n° AP132P) and were diluted 1/5000. The secondary antibodies used for immunofluorescence were: Alexa Fluor 488 anti-rabbit (Invitrogen, molecular probes, n°

A-21206) and Alexa Fluor 488 anti-mouse (Invitrogen, molecular probes, n° A-11029) and were diluted 1/200. F-actin was stained with phalloidin-TRITC (Sigma-Aldrich, n° P1951) and was diluted 1/1000.

Time-lapse microscopy

Multidimensional acquisitions were performed on an automated inverted microscope (Nikon Eclipse Ti, 10× lens) equipped with thermal, CO_2, and humidity control, using MetaMorph (Universal Imaging) software. Images were obtained every 3 minutes during 450 minutes. Up to 15 independent monolayers were imaged in parallel using a motorized XY stage.

Particle Imaging Velocimetry and strain rate calculation

Monolayer velocity fields were computed using a custom-made particle imaging velocimetry software. To reduce systematic biases in subpixel resolution and peak-locking effects, we implemented an iterative process (up to 4 iterations) based on a continuous window shift technique [13].

Strain-rate was $\dot{\varepsilon}_{xx}$ was calculated using the following expression [13, 65]:

$$\dot{\varepsilon}_{xx}=\frac{dV_x}{dx} \quad \text{Eq.2}$$

Traction Force microscopy

Traction forces were computed using Fourier Transform Traction Microscopy with finite gel thickness[36]. Gel displacements between any experimental time point and a reference image obtained after cell trypsinization were computed using particle imaging velocimetry software described above.

Monolayer Stress microscopy

In a 2D approximation, monolayer stress is fully captured by a tensor possessing two independent normal components (σ_{xx} and σ_{yy}) and two identical shear components (σ_{xy} and σ_{yx}) [6,14,33]. At every pixel of the monolayer, these four components of the stress tensor define two particular directions of the plane, one in which the normal stress is maximum and one in which it is minimum. These directions, which are mutually orthogonal, are called principal stress orientations, and the stress values in each principal orientation are called maximum (σ_{11}) and minimum (σ_{22}) stress components. The average normal stress is defined as $\sigma_n=(\sigma_{11}+\sigma_{22})/2$, while the maximum shear stress is defined as $\sigma_s=(\sigma_{11}-\sigma_{22})/2$. The spatial resolution and force precision of MSM are formally set by those in the original traction maps. How the reconstructed stress field is affected by the choice of boundary conditions and by the assumptions of continuity, incompressibility, and homogeneity was extensively studied elsewhere[13, 34].

Magnetocytometry

Bead pulling experiments were performed using magnetic tweezers as previously described [47, 66]. Briefly, 3μm diameter magnetic beads pre-coated with protein G (Novex)

Europe PMC Funders Author Manuscripts

were covalently coated with purified E-cadherin-Fc or P-cadherin-Fc proteins. Unless noted otherwise, the beads were first washed with NaPhosphate buffer (0.1M , pH 8), incubated with 20μg/ml of the Fc-Tagged proteins for 2hr, and then with crosslinking buffer for 1hr (25mM DMP, 0.2M triethanolamine, pH 8.2). The protein-coated beads were allowed to settle on a confluent monolayer of MCF10A cells for 30 minutes before starting the experiment. To measure the extent of reinforcement, a pulsatory force (0.2 nN unless stated otherwise) was applied to beads attached to cells. Bead movement in response to the pulsatory force was tracked using a custom-made tracking software. Stiffness of the cell-bead contact was calculated as the ratio between the amplitude of the applied force and that of the observed bead oscillation. The magnetic force generated by the magnet is restricted to the close proximity of the magnet tip[47, 66]. All beads probed from one sample were selected far enough from each other so that they only experienced the forcing protocol once.

Vinculin recruitment was measured using Magnetic Twisting Cytometry as previously described[50].

Averaging

Physical properties of cells and cell monolayers often exhibit broad non-Gaussian distributions with log-normal or exponential tails[67]. To avoid potential averaging artifacts caused by extreme data in these tails, we first computed the median -rather than the mean- of any physical property across space (Supplementary Note). We then averaged medians over experimental repeats and/or time. In the case of cell velocities, which average to roughly zero due to the symmetry of monolayer expansion, we computed the median of absolute values.

Computation of z-scores

The z-score (or standard score in statistics) is defined as the signed number of standard deviations an observed quantity deviates from the mean of that quantity[68]. In the context of this study, the z-score of a quantity x (a physical property in Fig. 5a or a protein concentration in Fig. 6a) in response to a siRNA perturbation is defined as:

$$Z = \frac{\bar{x} - \overline{x_c}}{\sigma_c} \quad \text{Eq.3}$$

where $\bar{x}$ is the mean of x under the siRNA perturbation, $\overline{x_c}$ is the mean of x under control conditions, and σ_c is the standard deviation of x under control conditions.

Computation of correlation matrices

As a measure of correlation we used cosine similarity between pairs of vectors containing z-scores of physical properties. Consider a matrix Z containing the z-scores of n physical properties under m siRNA perturbations (m rows and n columns). Each column of the matrix defines a m-dimensional vector $\vec{P}$ that contains the z-scores of one physical property. To assess the correlation between two physical properties i and j we computed the cosine of the

angle θ_{ij} between the vectors $\overrightarrow{P_i}$ and $\overrightarrow{P_j}$ (vectors that contain the z-scores of properties *i* and *j*):

$$\cos(\theta_{ij}) = \frac{\overrightarrow{P_i} \cdot \overrightarrow{P_j}}{\|P_i\| \, \|P_j\|} \quad \text{Eq.4}$$

When repeated over each possible pair of physical properties, this operation yields a $n \times n$ correlation matrix C in which each element is defined as $C_{ij} = \cos(\theta_{ij})$. This matrix is shown in Fig. 5b. In a similar way, we also computed a $q \times q$ correlation matrix of siRNA perturbations (Fig. 5c) and a $k \times k$ correlation matrix of protein concentrations (Fig. 6b).

Unsupervised clustering analysis

Unsupervised clustering analysis was performed as described in Sales-Pardo et al [41] (see also Supplementary Note). Briefly, we first ordered the correlation matrix to place high correlation values close to the diagonal and low correlation values close to the matrix edges. Second, we obtained clusters by identifying diagonal blocks containing elements of high correlation. To this end, we assumed a matrix model that is block diagonal in which matrix elements in each block are equal and off-diagonal elements are also equal. We then obtained the block diagonal model that fits best our ordered matrix according to the Bayesian Information Criterion.

Leave-one-out cross-validation

To select predictive models and assess their predictive power we performed a LOOCV analysis[69]. We proceeded as follows. For a given physical property X and a given silencing condition *k*, we fit the linear model (Eq. 1 for one protein, or a linear combination of N proteins for N-protein models) using the values of X under all conditions except *k* (that is, we determine A and B_i leaving condition *k* out). Then we used the fitted model to make a prediction of X under condition *k*. We repeated the same operation for all conditions and computed the mean squared error of the predictions. The most predictive model was then the one that yielded the smallest mean squared error. To establish significance of the predictions and ensure that low prediction errors were not merely an outcome of multiple-testing, we run randomization tests on the values of the physical properties and kept only models whose prediction error was significantly low at a 5% level. This approach is typically used to avoid overfitting when the number of potential explanatory variables (in our case protein concentrations) is of the order of the number of conditions (in our case siRNAs) under which predictions are sought.

Code availability

Computer codes developed for this study can be made available upon request to the corresponding author.

Repeatability of experiments

All immunostaining experiments were performed on at least three independent cell culture preparations, imaged over two or more imaging sessions. Magnetic tweezers experiments were performed in three independent cell culture preparations. Western blot experiments were performed on three independent transfections. RT-PCR experiments were run in triplicate and performed on at least two independent transfections.

Supplementary Material

Refer to Web version on PubMed Central for supplementary material.

Acknowledgements

We thank F. Supek, B. Lehner, A. Brugués and R. Vincent for discussions, R. Zaidel-Bar for sharing unpublished data, and E. Sahai for contributing reagents. This research was supported by the European Research Council (StG-242993 and CoG - 616480 to XT), the 7th European Community Framework Programme (PCIG10-GA-2011-303848 to PR, PIRG-GA-2010-277166 to RG, PIRG-GA-2010-268342 to MS, FET Grant 317532 to MS and RG), the Spanish Ministerio de Economía y Comptetitividad (BFU2012-38146 to XT, FIS2010-18639 to MS and RG, BFU2011-23111 to PR. Juan de la Cierva Fellowship JCI-2012-15123 to VC), the National Institutes of Health (R01HL107561 to XT), and the James S. McDonnell Foundation (RG and MS).

References

1. Friedl P, Gilmour D. Collective cell migration in morphogenesis, regeneration and cancer. Nature reviews. Molecular cell biology. 2009; 10:445–457. [PubMed: 19546857]
2. Weber GF, Bjerke MA, DeSimone DW. A mechanoresponsive cadherin-keratin complex directs polarized protrusive behavior and collective cell migration. Developmental cell. 2012; 22:104–115. [PubMed: 22169071]
3. Heisenberg CP, Bellaiche Y. Forces in tissue morphogenesis and patterning. Cell. 2013; 153:948–962. [PubMed: 23706734]
4. Leckband DE, le Duc Q, Wang N, de Rooij J. Mechanotransduction at cadherin-mediated adhesions. Current opinion in cell biology. 2011; 23:523–530. [PubMed: 21890337]
5. Budnar S, Yap AS. A mechanobiological perspective on cadherins and the actin-myosin cytoskeleton. F1000Prime Rep. 2013; 5:35. [PubMed: 24049639]
6. Tambe DT, et al. Collective cell guidance by cooperative intercellular forces. Nature materials. 2011; 10:469–475. [PubMed: 21602808]
7. Theveneau E, et al. Chase-and-run between adjacent cell populations promotes directional collective migration. Nature cell biology. 2013; 15:763–772. [PubMed: 23770678]
8. Campinho P, et al. Tension-oriented cell divisions limit anisotropic tissue tension in epithelial spreading during zebrafish epiboly. Nature cell biology. 2013; 15:1405–1414. [PubMed: 24212092]
9. Bosveld F, et al. Mechanical control of morphogenesis by Fat/Dachsous/Four-jointed planar cell polarity pathway. Science. 2012; 336:724–727. [PubMed: 22499807]
10. Legoff L, Rouault H, Lecuit T. A global pattern of mechanical stress polarizes cell divisions and cell shape in the growing Drosophila wing disc. Development. 2013; 140:4051–4059. (Cambridge, England). [PubMed: 24046320]
11. Brugués A, et al. Forces driving epithelial wound healing. Nature Physics. 2014; 10:683–690. [PubMed: 27340423]
12. Rauzi M, Lenne PF, Lecuit T. Planar polarized actomyosin contractile flows control epithelial junction remodelling. Nature. 2010; 468:1110–1114. [PubMed: 21068726]
13. Serra-Picamal X, et al. Mechanical waves during tissue expansion. Nature Physics. 2012; 8:628–634.
14. Foty RA, Steinberg MS. The differential adhesion hypothesis: a direct evaluation. Developmental biology. 2005; 278:255–263. [PubMed: 15649477]

15. Borghi N, et al. E-cadherin is under constitutive actomyosin-generated tension that is increased at cell-cell contacts upon externally applied stretch. Proc Natl Acad Sci U S A. 2012; 109:12568–12573. [PubMed: 22802638]
16. Maitre JL, Heisenberg CP. Three functions of cadherins in cell adhesion. Curr Biol. 2013; 23:R626–633. [PubMed: 23885883]
17. Zaidel-Bar R. Cadherin adhesome at a glance. Journal of cell science. 2013; 126:373–378. [PubMed: 23547085]
18. Nieman MT, Prudoff RS, Johnson KR, Wheelock MJ. N-cadherin promotes motility in human breast cancer cells regardless of their E-cadherin expression. The Journal of cell biology. 1999; 147:631–644. [PubMed: 10545506]
19. Ribeiro AS, et al. Extracellular cleavage and shedding of P-cadherin: a mechanism underlying the invasive behaviour of breast cancer cells. Oncogene. 2010; 29:392–402. [PubMed: 19901964]
20. Batlle E, et al. The transcription factor snail is a repressor of E-cadherin gene expression in epithelial tumour cells. Nature cell biology. 2000; 2:84–89. [PubMed: 10655587]
21. Kumper S, Ridley AJ. p120ctn and P-cadherin but not E-cadherin regulate cell motility and invasion of DU145 prostate cancer cells. PloS one. 2010; 5:e11801. [PubMed: 20668551]
22. Ribeiro AS, et al. P-cadherin functional role is dependent on E-cadherin cellular context: a proof of concept using the breast cancer model. The Journal of pathology. 2013; 229:705–718. [PubMed: 23180380]
23. Tabdili H, et al. Cadherin-dependent mechanotransduction depends on ligand identity but not affinity. Journal of cell science. 2012; 125:4362–4371. [PubMed: 22718345]
24. Buckley CD, et al. Cell adhesion. The minimal cadherin-catenin complex binds to actin filaments under force. Science. 2014; 346:1254211. [PubMed: 25359979]
25. Abe K, Takeichi M. EPLIN mediates linkage of the cadherin catenin complex to F-actin and stabilizes the circumferential actin belt. Proc Natl Acad Sci U S A. 2008; 105:13–19. [PubMed: 18093941]
26. Yamada S, Pokutta S, Drees F, Weis WI, Nelson WJ. Deconstructing the cadherin-catenin-actin complex. Cell. 2005; 123:889–901. [PubMed: 16325582]
27. Runkle EA, Mu D. Tight junction proteins: from barrier to tumorigenesis. Cancer letters. 2013; 337:41–48. [PubMed: 23743355]
28. Harris AR, et al. Characterizing the mechanics of cultured cell monolayers. Proc Natl Acad Sci U S A. 2012; 109:16449–16454. [PubMed: 22991459]
29. Herrmann H, Bar H, Kreplak L, Strelkov SV, Aebi U. Intermediate filaments: from cell architecture to nanomechanics. Nature reviews. Molecular cell biology. 2007; 8:562–573. [PubMed: 17551517]
30. Wang N, Stamenovic D. Contribution of intermediate filaments to cell stiffness, stiffening, and growth. American journal of physiology. 2000; 279:C188–194. [PubMed: 10898730]
31. Bao L, Sachs F, Dahl G. Connexins are mechanosensitive. American journal of physiology. 2004; 287:C1389–1395. [PubMed: 15475518]
32. Poujade M, et al. Collective migration of an epithelial monolayer in response to a model wound. Proc Natl Acad Sci U S A. 2007; 104:15988–15993. [PubMed: 17905871]
33. Hur SS, et al. Roles of cell confluency and fluid shear in 3-dimensional intracellular forces in endothelial cells. Proc Natl Acad Sci U S A. 2012; 109:11110–11115. [PubMed: 22665785]
34. Tambe DT, et al. Monolayer stress microscopy: limitations, artifacts, and accuracy of recovered intercellular stresses. PloS one. 2013; 8:e55172. [PubMed: 23468843]
35. Trepat X, Fredberg JJ. Plithotaxis and emergent dynamics in collective cellular migration. Trends Cell Biol. 2012; 21:638–646. [PubMed: 21784638]
36. Trepat X, et al. Physical forces during collective cell migration. Nature Physics. 2009; 5:426–430.
37. Liu Z, et al. Mechanical tugging force regulates the size of cell-cell junctions. Proc Natl Acad Sci U S A. 2010; 107:9944–9949. [PubMed: 20463286]
38. Maruthamuthu V, Sabass B, Schwarz US, Gardel ML. Cell-ECM traction force modulates endogenous tension at cell-cell contacts. Proc Natl Acad Sci U S A. 2011; 108:4708–4713. [PubMed: 21383129]

39. Ng MR, Besser A, Brugge JS, Danuser G. Mapping the dynamics of force transduction at cell-cell junctions of epithelial clusters. eLife. 2014; 4
40. Simpson KJ, et al. Identification of genes that regulate epithelial cell migration using an siRNA screening approach. Nature cell biology. 2008; 10:1027–1038. [PubMed: 19160483]
41. Sales-Pardo M, Guimera R, Moreira AA, Amaral LA. Extracting the hierarchical organization of complex systems. Proc Natl Acad Sci U S A. 2007; 104:15224–15229. [PubMed: 17881571]
42. Fanning AS, Van Itallie CM, Anderson JM. Zonula occludens-1 and -2 regulate apical cell structure and the zonula adherens cytoskeleton in polarized epithelia. Molecular biology of the cell. 2012; 23:577–590. [PubMed: 22190737]
43. Tuomi S, et al. PKCepsilon regulation of an alpha5 integrin-ZO-1 complex controls lamellae formation in migrating cancer cells. Science signaling. 2009; 2:ra32. [PubMed: 19567915]
44. Bausch AR, Moller W, Sackmann E. Measurement of local viscoelasticity and forces in living cells by magnetic tweezers. Biophysical journal. 1999; 76:573–579. [PubMed: 9876170]
45. le Duc Q, et al. Vinculin potentiates E-cadherin mechanosensing and is recruited to actin-anchored sites within adherens junctions in a myosin II-dependent manner. The Journal of cell biology. 2010; 189:1107–1115. [PubMed: 20584916]
46. Riveline D, et al. Focal contacts as mechanosensors: externally applied local mechanical force induces growth of focal contacts by an mDia1-dependent and ROCK-independent mechanism. The Journal of cell biology. 2001; 153:1175–1186. [PubMed: 11402062]
47. Roca-Cusachs P, Gauthier NC, Del Rio A, Sheetz MP. Clustering of alpha(5)beta(1) integrins determines adhesion strength whereas alpha(v)beta(3) and talin enable mechanotransduction. Proc Natl Acad Sci U S A. 2009; 106:16245–16250. [PubMed: 19805288]
48. Yonemura S, Wada Y, Watanabe T, Nagafuchi A, Shibata M. alpha-Catenin as a tension transducer that induces adherens junction development. Nature cell biology. 2010; 12:533–542. [PubMed: 20453849]
49. Yao M, et al. Force-dependent conformational switch of alpha-catenin controls vinculin binding. Nature communications. 2014; 5:4525.
50. Barry AK, et al. alpha-catenin cytomechanics--role in cadherin-dependent adhesion and mechanotransduction. Journal of cell science. 2014; 127:1779–1791. [PubMed: 24522187]
51. Cano A, et al. The transcription factor snail controls epithelial-mesenchymal transitions by repressing E-cadherin expression. Nature cell biology. 2000; 2:76–83. [PubMed: 10655586]
52. Thiery JP, Acloque H, Huang RY, Nieto MA. Epithelial-mesenchymal transitions in development and disease. Cell. 2009; 139:871–890. [PubMed: 19945376]
53. Stark C, et al. BioGRID: a general repository for interaction datasets. Nucleic acids research. 2006; 34:D535–539. [PubMed: 16381927]
54. Albergaria A, et al. P-cadherin role in normal breast development and cancer. The International journal of developmental biology. 2011; 55:811–822. [PubMed: 22161837]
55. van Roy F. Beyond E-cadherin: roles of other cadherin superfamily members in cancer. Nature reviews. Cancer. 2014; 14:121–134. [PubMed: 24442140]
56. Vleminckx K, Vakaet L Jr. Mareel M, Fiers W, van Roy F. Genetic manipulation of E-cadherin expression by epithelial tumor cells reveals an invasion suppressor role. Cell. 1991; 66:107–119. [PubMed: 2070412]
57. Wong AS, Gumbiner BM. Adhesion-independent mechanism for suppression of tumor cell invasion by E-cadherin. The Journal of cell biology. 2003; 161:1191–1203. [PubMed: 12810698]
58. Van Marck V, et al. P-cadherin promotes cell-cell adhesion and counteracts invasion in human melanoma. Cancer Res. 2005; 65:8774–8783. [PubMed: 16204047]
59. Jacobs K, et al. P-cadherin counteracts myosin II-B function: implications in melanoma progression. Molecular cancer. 2010; 9:255. [PubMed: 20860798]
60. Bechhoefer J. Feedback for physicists: A tutorial essay on control. Reviews of Modern Physics. 2005; 77:783–836.
61. Cloutier M, Wellstead P. The control systems structures of energy metabolism. Journal of the Royal Society, Interface / the Royal Society. 2010; 7:651–665.

62. Kandow CE, Georges PC, Janmey PA, Beningo KA. Polyacrylamide hydrogels for cell mechanics: steps toward optimization and alternative uses. Methods in cell biology. 2007; 83:29–46. [PubMed: 17613303]

63. Yeung T, et al. Effects of substrate stiffness on cell morphology, cytoskeletal structure, and adhesion. Cell Motil Cytoskeleton. 2005; 60:24–34. [PubMed: 15573414]

64. Ostuni E, Kane RS, Chen CS, Ingber DE, Whitesides GM. Patterning Mammalian Cells Using Elastomeric Membranes. Langmuir. 2000; 16:7811.

65. Blanchard GB, et al. Tissue tectonics: morphogenetic strain rates, cell shape change and intercalation. Nature methods. 2009; 6:458–464. [PubMed: 19412170]

66. Roca-Cusachs P, et al. Integrin-dependent force transmission to the extracellular matrix by alpha-actinin triggers adhesion maturation. Proc Natl Acad Sci U S A. 2013; 110:E1361–1370. [PubMed: 23515331]

67. Fabry B, et al. Time scale and other invariants of integrative mechanical behavior in living cells. Physical review. 2003; 68:041914. [PubMed: 14682980]

68. Birmingham A, et al. Statistical methods for analysis of high-throughput RNA interference screens. Nature methods. 2009; 6:569–575. [PubMed: 19644458]

69. Simon, R. Resampling Strategies for Model Assessment and Selection : Leave-One-Out-Cross-Validation. In: Dubitzky, W.; Granzow, M.; Berrar, DP., editors. Fundamentals of Data Mining in Genomics and Proteomics. Springer Science+Business Media; 2007. p. 177-178.

Europe PMC Funders Author Manuscripts

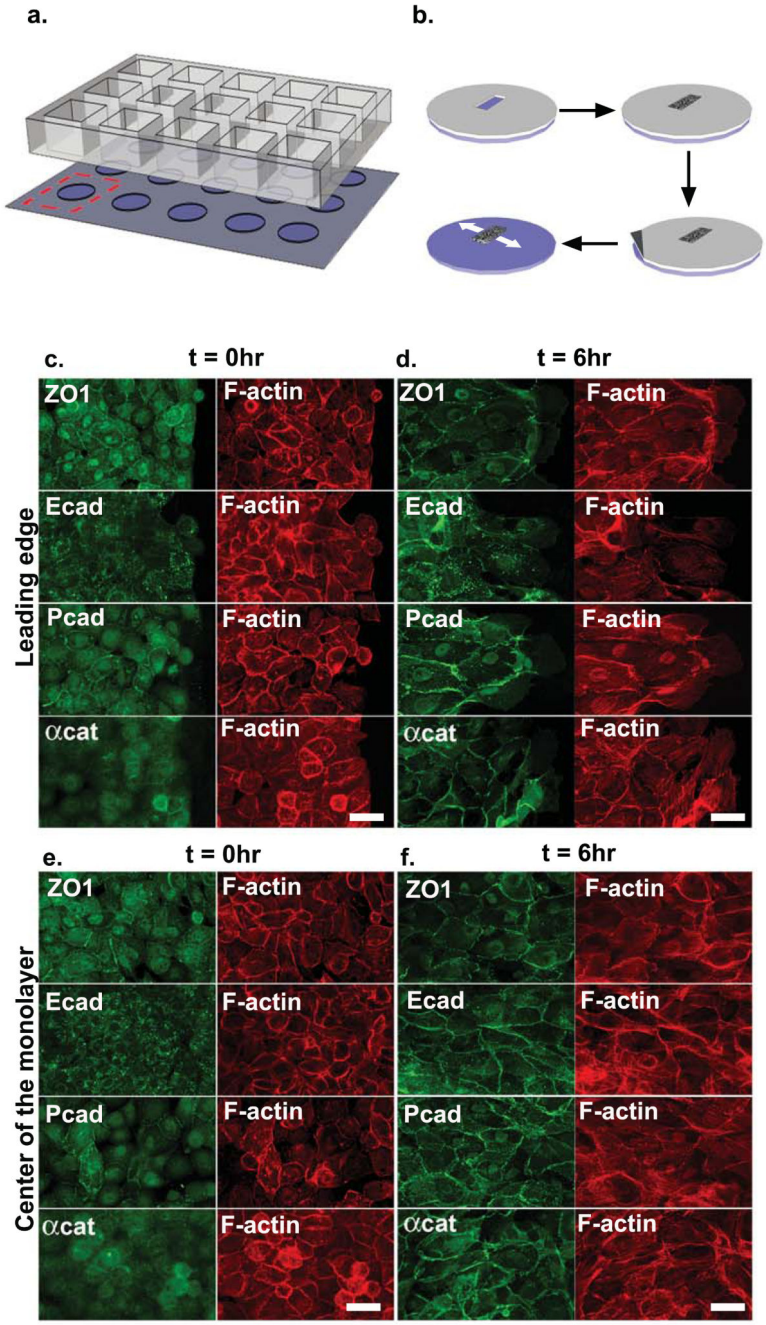

Figure 1. Intercellular cohesiveness increases with monolayer expansion

Scheme of the experimental setup. (a) A large glass slide was attached to a custom-made PDMS frame containing 15 openings that served as individual wells. Each well contained a collagen I-coated micropatterned gel. (b) A PDMS membrane with a rectangular opening was deposited on top of each polyacrylamide gel. Next, cells were seeded on top of each gel and allowed to adhere. After 5 hours, the PDMS membranes were removed. (c-f) Localization of ZO-1, E-cadherin, P-cadherin, α-catenin, and F-actin at the leading edge (c,d) and center (e,f) of the monolayer at t=0hr (c,e) and t=6hr (d,f). Scale bar 20μm.

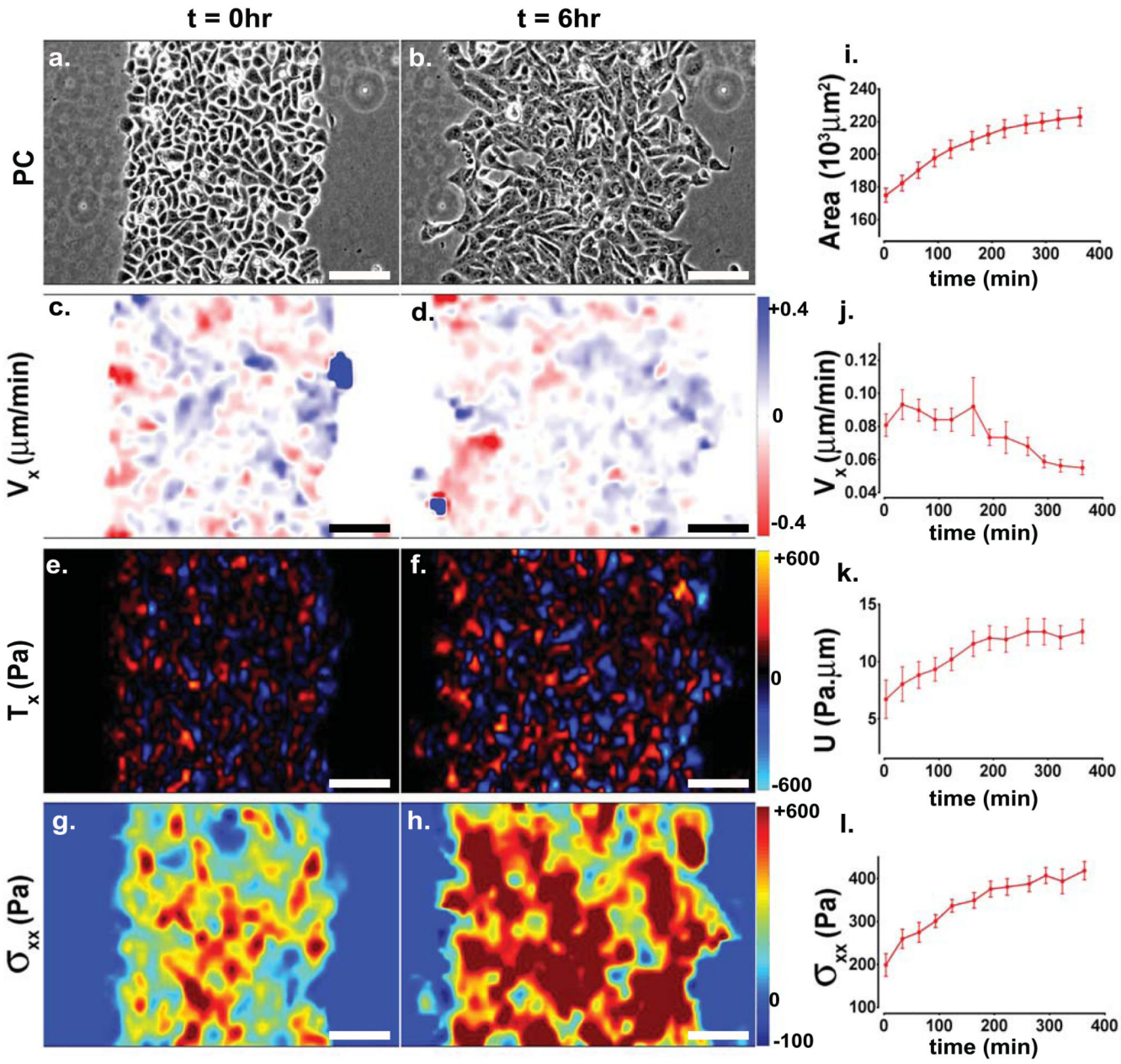

Figure 2. As the monolayer increases its cohesiveness, cell migration slows down and physical forces buildup

Phase contrast images (a,b), maps of cell velocities (c,d), maps of traction forces (e,f), and maps of monolayer tension (g,h) at t=0hr (a,c,e,g) and t=6hr (b,d,f,h). Time evolution of monolayer area (i), cell velocity (j), strain energy density (k), and monolayer tension (l). Scale bar, 100μm. Data are presented as mean ± SEM (n = 13 independent cell monolayers assessed over 10 experiments).

Europe PMC Funders Author Manuscripts

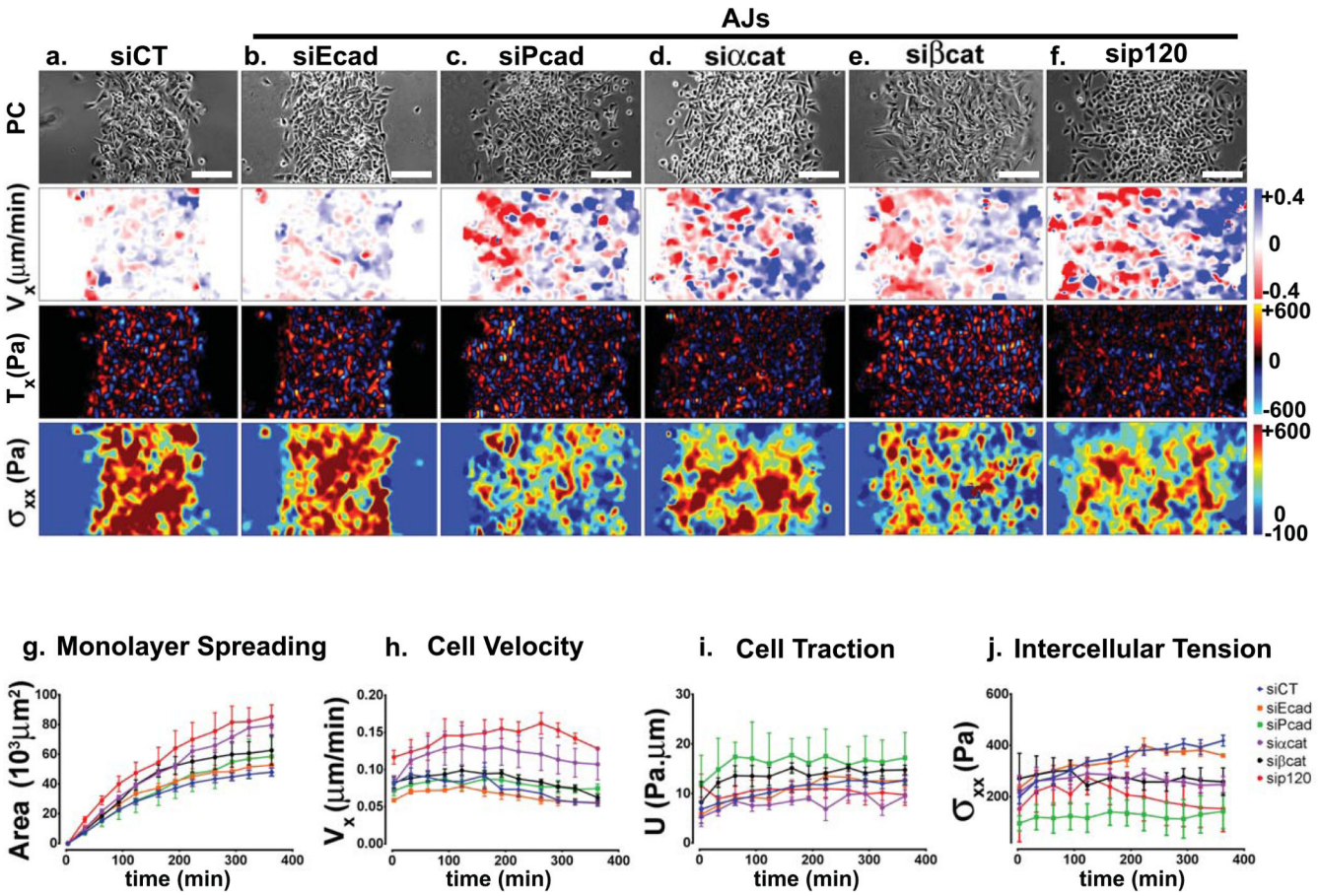

Figure 3. Downregulation of adherens junctions alters monolayer dynamics

Representative maps showing the effect of siRNAs on monolayer dynamics after 8hr of expansion. For each siRNA, each row displays phase contrast images (first row), monolayer velocity (second row), traction force (third row), and intercellular tension (forth row). Panels show the control case (a) and selected siRNAs targeting adherens junctions (b-f). Additional time points and siRNA perturbations are shown in Supplementary Figs. 2-4. Time evolution of monolayer area (shown as the increase from the initial area) (g), cell velocity (h), strain energy density (i), and intercellular tension (j) for the control case and siRNAs shown in panels b-f. The time evolution of physical properties in response to all siRNAs is shown in Supplementary Fig. 8. Scale bar, 100μm. Data are presented as mean ± SEM. n=13 independent cell monolayers (siCT), n=4 independent cell monolayers (siαcat, siPcad, sip120), n=3 independent cell monolayers (siEcad, siβcat); monolayers were assessed over 10 experiments (siCT), 3 experiments (siαcat), 2 experiments (siPcad, sip120, siEcad, siβcat).

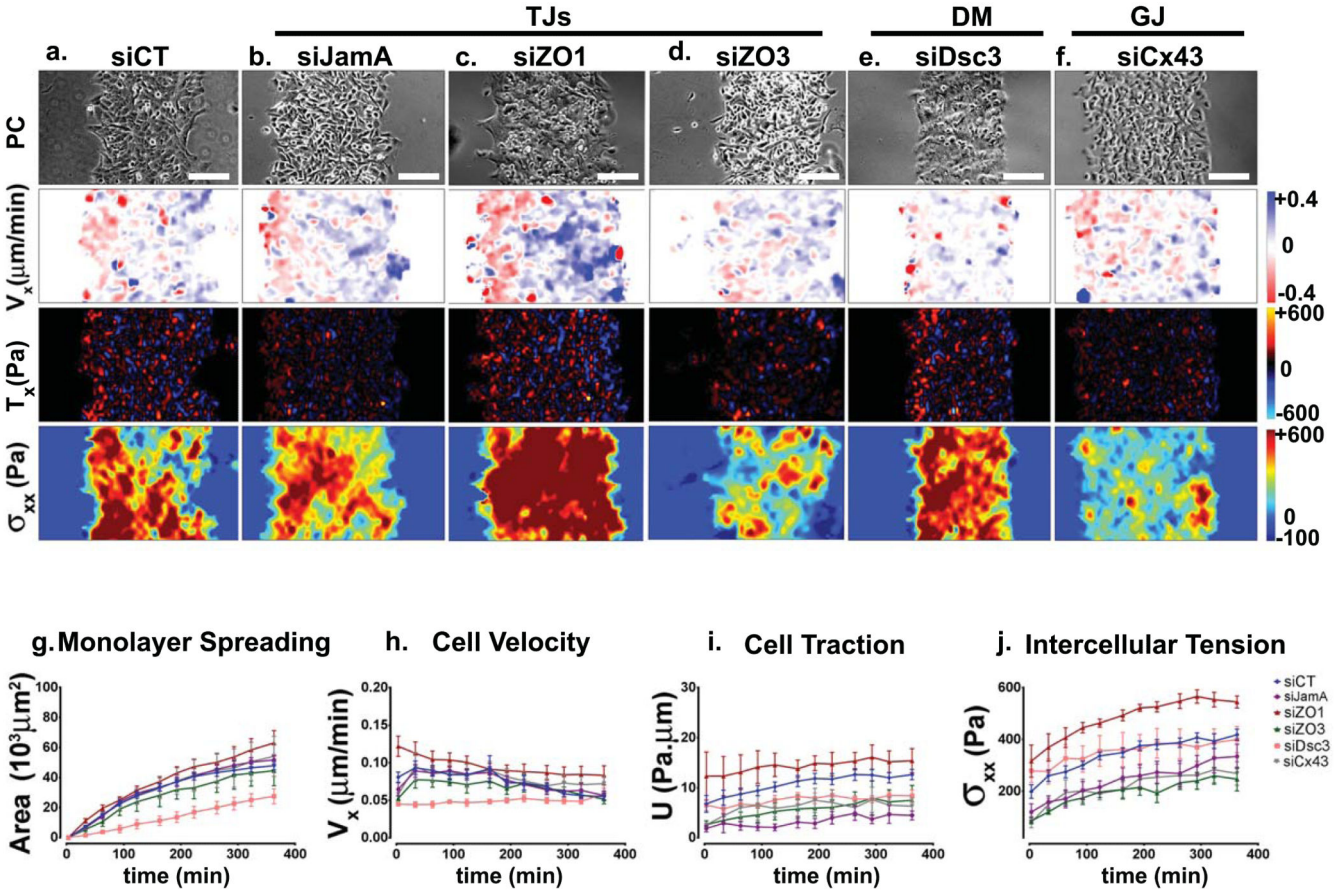

Figure 4. Downregulation of tight junctions, desmosomes, and gap junctions alters monolayer dynamics

Representative maps showing the effect of siRNAs on monolayer dynamics after 8hr of expansion. For each siRNA, each row displays phase contrast images (first row), monolayer velocity (second row), traction force (third row), and intercellular tension (forth row). Panels show the control case (a) and selected siRNAs targeting tight junctions (b-d), desmosomes (e), and gap junctions (f). Additional time points and siRNA perturbations are shown in Supplementary Figs. 5-7. Time evolution of monolayer area (shown as the increase from the initial area) (g), cell velocity (h), strain energy density (i), and intercellular tension (j) for the control case and the 5 siRNAs shown in panels b-f. The time evolution of physical properties in response to all siRNAs is shown in Supplementary Fig. 8. Scale bar, 100μm. Data are presented as mean ± SEM. n=13 independent cell monolayers (siCT), n=3 independent cell monolayers (siJamA, siZO3), n=4 independent cell monolayers (siCx43), n=5 independent cell monolayers (siDSC3), n=7 independent cell monolayers (siZO1); monolayers were assessed over 10 experiments (siCT), 3 experiments (siCx43, siDSC3), 2 experiments (siJamA, siZO3, siZO1).

Europe PMC Funders Author Manuscripts

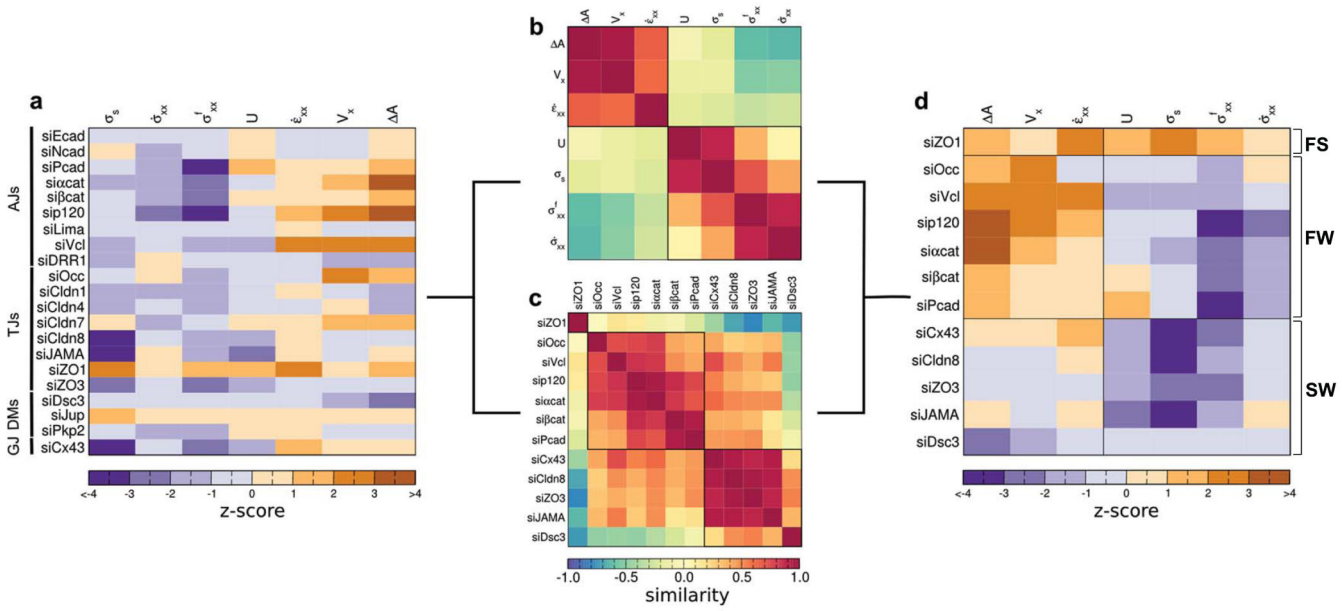

Figure 5. Cell monolayers with perturbed cell-cell adhesions exhibit distinct mechanical phenotypes

(a) Effect of siRNAs on physical properties expressed in terms of their z-scores (see Supplementary Table 1 and Supplementary Note for a description of each physical property). (b) Correlation between physical properties computed as the cosine similarity between all possible pairs of columns in panel (a). (c) Correlation between siRNAs computed as the cosine similarity between all possible pairs of rows in panel (a). An unsupervised clustering algorithm was used to order rows and columns in panels (b) and (c) and to identify clusters whose separation is marked with black lines. (d) Reorganization of panel (a) into phenotypic clusters according to the unsupervised analysis of correlation matrices (b) and (c). FS (Fast/Strong), FW (Fast/Weak), SW (Steady/Weak).

Europe PMC Funders Author Manuscripts

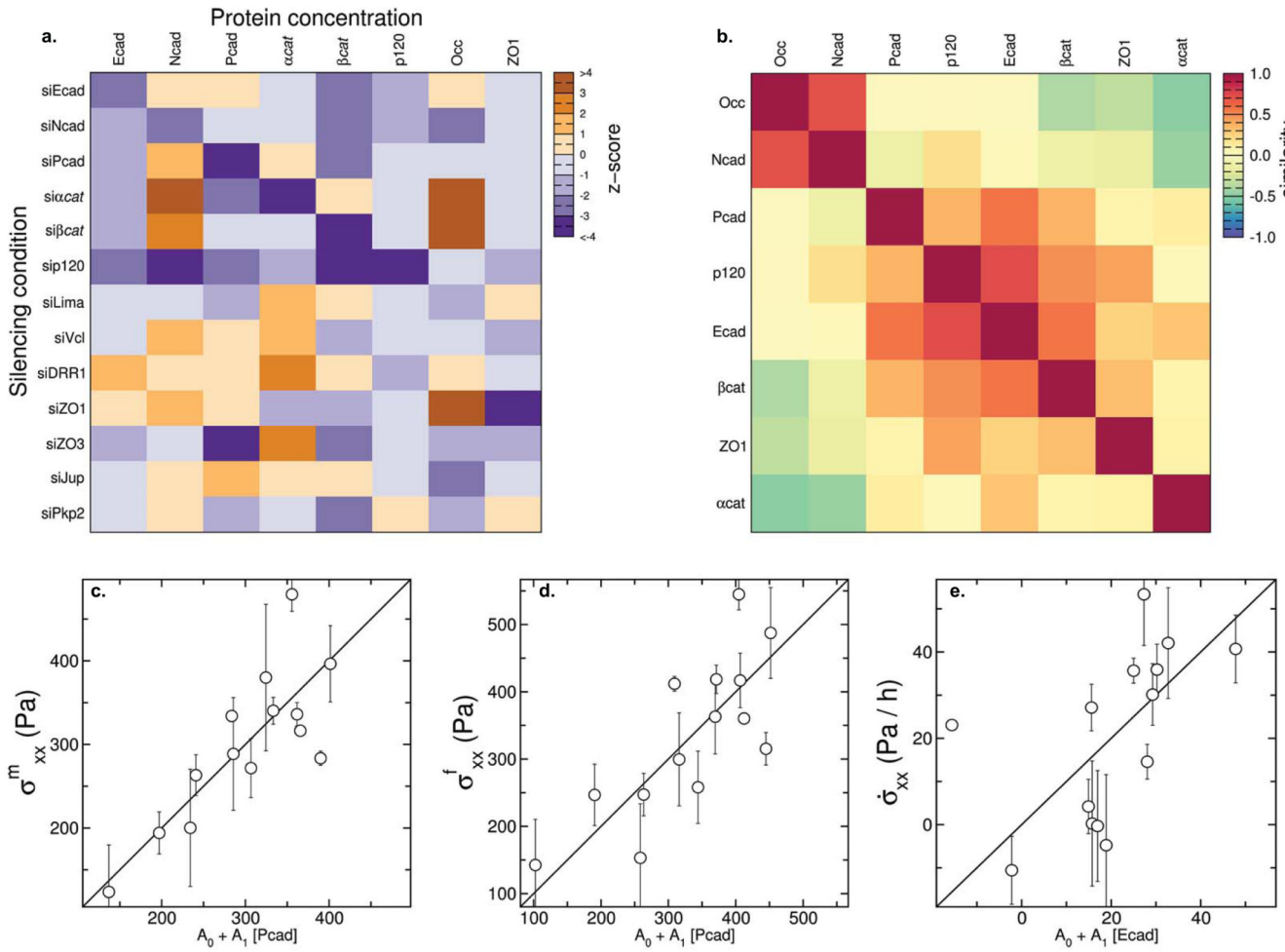

Figure 6. Protein concentrations predict intercellular forces and their buildup rate

(a) z-scores of protein concentrations in response to siRNA perturbations. (b) Correlation between protein expression patterns computed as the cosine similarity between columns in panel (a). (c) The concentration of P-cadherin predicts average intercellular tension. (d) The concentration of P-cadherin predicts intercellular tension at the end of the experiment. (e) The concentration of E-cadherin predicts the rate of intercellular tension buildup. The *x*-axis in panels c-e shows the values predicted by the 1-protein models whereas the y-axis shows the experimental values. Each data point corresponds to one siRNA perturbation. Error bars in panels are SEM. n=13 independent cell monolayers (siCT), n=7 independent cell monolayers (siZO1), n=4 independent cell monolayers (siPcad, sip120, siVcl, siJup, siαcat), n=3 independent cell monolayers (siEcad, siNcad, siβcat, siLima, siDRR1, siZO3, siPkp2); monolayers were assessed over 10 experiments (siCT), 3 experiments (siαcat), 2 experiments (siEcad, siNcad, siβcat, siLima, siDRR1, siZO3, siPkp2, siPcad, sip120, siVcl, siJup, siZO1). All predictions displayed in panels c-e were significant to $p<0.05$ using a leave-one-out cross-validation. See Supplementary Table 2 for values of prediction errors. See Supplementary Table 3 for predictions by N-protein models.

Europe PMC Funders Author Manuscripts

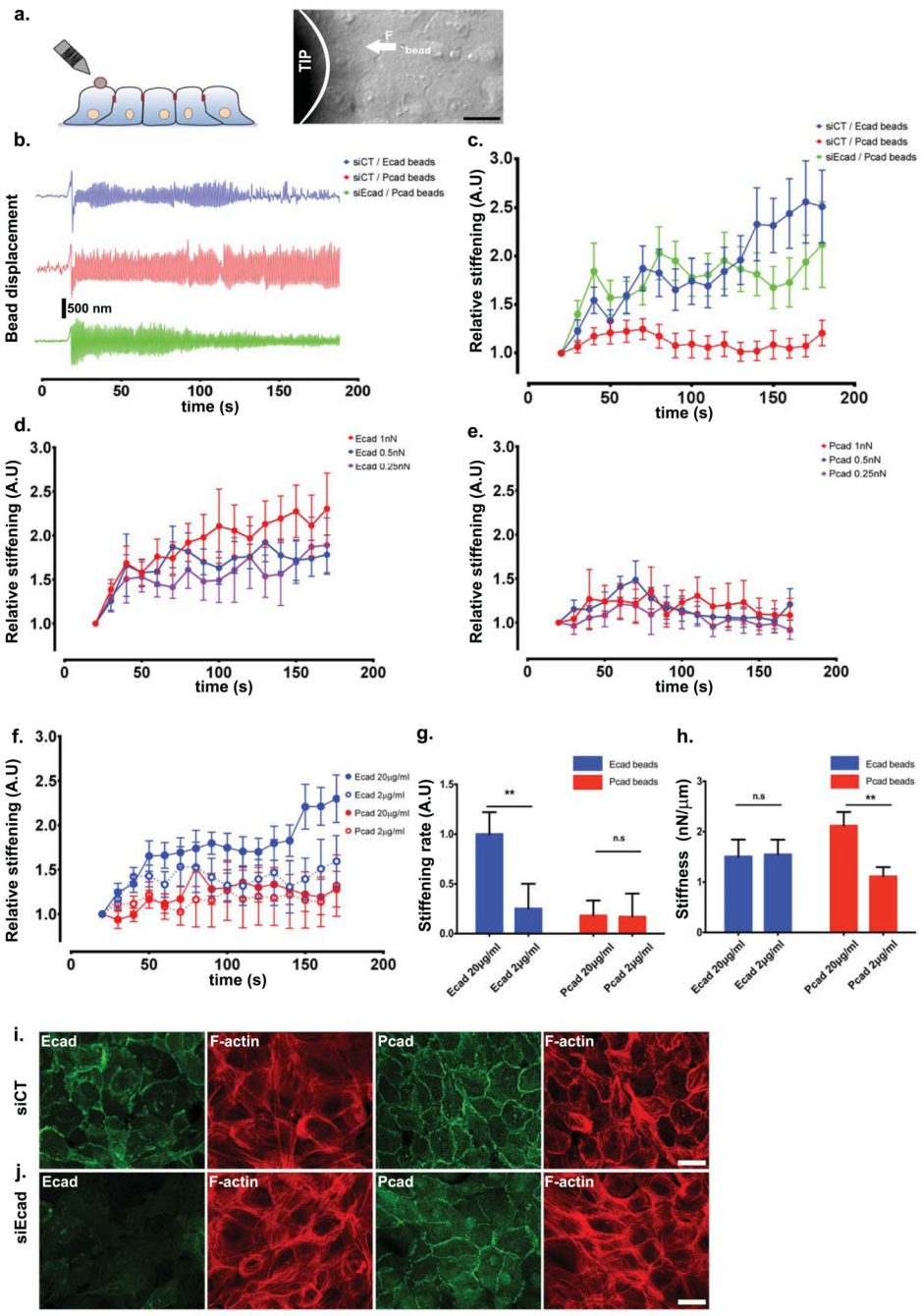

Figure 7. Force applied to E-cadherin triggers reinforcement feedback loops whereas force applied to P-cadherin does not

(a) Experimental setup: magnetic beads coated with E-cadherin or P-cadherin were attached to the apical surface of MCF10A monolayers and subjected to a series force pulses using magnetic tweezers. (b) Representative examples of bead displacements for P-cadherin-coated beads bound to control cells (red), E-cadherin-coated beads bound to control cells (blue), and P-cadherin-coated beads bound to siEcad cells (green). (c) Relative stiffening of the cell-bead contact for P-cadherin-coated beads bound to control cells (red, n=22 beads pooled from 9 independent wells), E-cadherin-coated beads bound to control cells (blue,

n=26 beads pooled from 9 independent wells), and P-cadherin-coated beads bound to cells depleted of E-cadherin (green, n=23 beads pooled from 9 independent wells). (d) Relative stiffening of the junction between cells and beads coated with E-cadherin in response to oscillatory forces of amplitude 0.25 nN (purple, n=22 beads pooled from 9 independent wells), 0.5 nN (blue, n=20 beads pooled from 9 independent wells) and 1 nN (red, n=13 beads pooled from 9 independent wells). (e) Relative stiffening of the junction between cells and beads coated with P-cadherin in response to oscillatory forces of amplitude 0.25 nN (purple, n=16 beads pooled from 9 independent wells), 0.5 nN (blue, n=16 beads pooled from 9 independent wells) and 1 nN (red, n=15 beads pooled from 9 independent wells). (f) Relative stiffening of the junction between cells and beads coated with E-cadherin (blue) and P-cadherin (red) using coating solutions of 2 μg/ml (open symbols) or 20 μg/ml (filled symbols). (g) Stiffening rate (slope of curves in panel f) of the cell-bead contact. (h) Initial stiffness of the cell bead contact. In c-h data are represented as mean+SEM. * indicates $p<0.05$, *** indicates $p<0.001$ (Mann-Whitney Rank Sum t-test). n.s. indicates non-significant comparisons. In (f-h) n=17 beads pooled from 6 independent wells for Ecad 20μg/ml; n=16 beads pooled from 6 independent wells for Ecad 2μg/ml; n=16 beads pooled from 6 independent wells for Pcad 20μg/ml; n=17 beads pooled from 6 independent wells for Pcad 2μg/ml. (i) Staining of E-cadherin, P-cadherin, and F-actin (phalloidin) under control conditions and (j) after E-cadherin knock down. Scale bar, 20 μm (a, i-j).

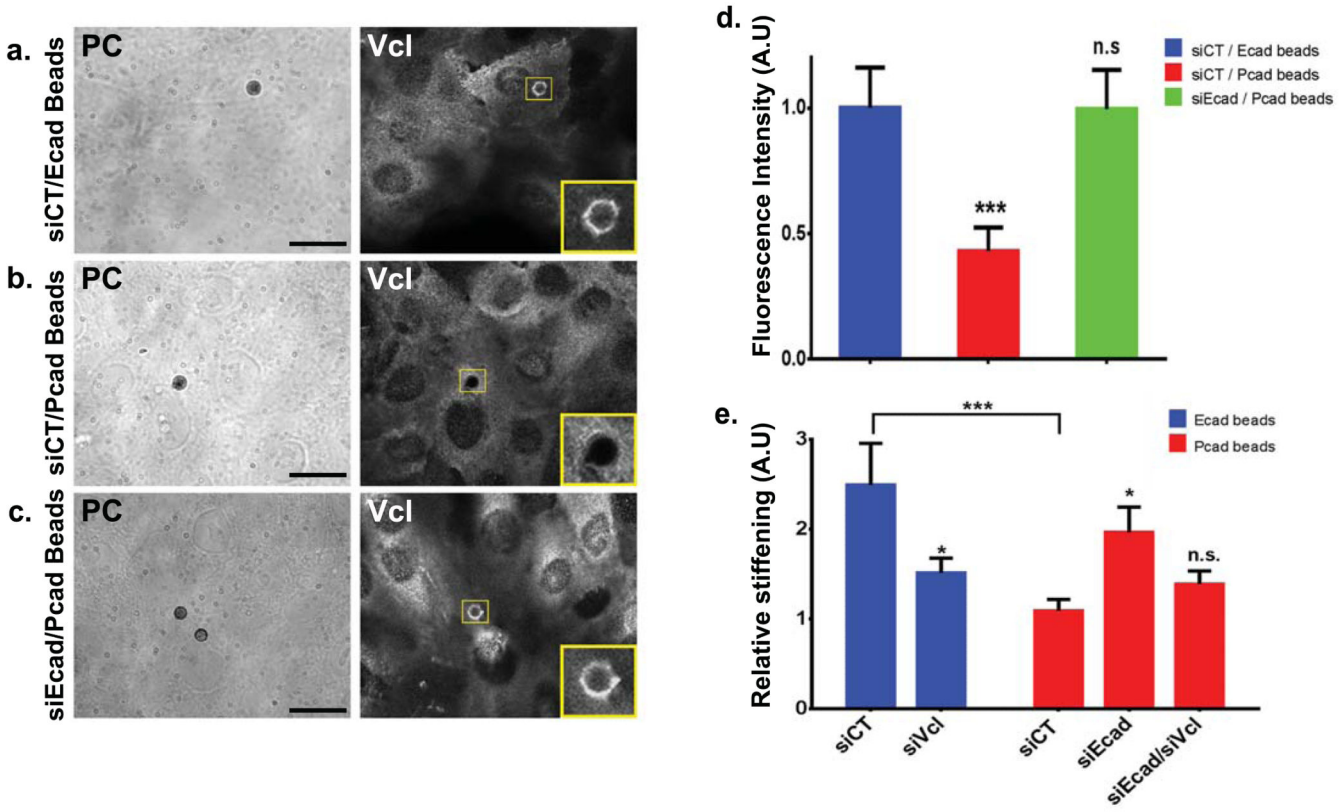

Figure 8. Vinculin is involved in mechanotransduction through P-cadherin and E-cadherin

(a) Phase contrast image (left) and staining (right) of vinculin (Vcl) after force application at the contact between control cells and beads coated with E-cadherin. (b) Phase contrast image (left) and staining (right) of vinculin after force application at the contact between control cells and beads coated with P-cadherin. (c) Phase contrast image (left) and staining (right) of vinculin (Vcl) after force application at the contact between cells depleted of E-cadherin and beads coated with P-cadherin. (d) Vinculin recruitment at the cell-bead contact for E-cadherin-coated beads bound to control cells (blue, n=25 beads pooled from 12 independent wells), P-cadherin coated beads bound to control cells (red, n=28 beads pooled from 12 independent wells) and P-cadherin coated beads bound to cells depleted of E-cadherin (green, n=20 beads pooled from 9 independent wells). Data are presented as mean ± SEM (normalized to Vcl recruitment in E-cadherin-coated beads bound to control cells) (e) Relative stiffening at the end of bead pulling assays (180 s). Beads were coated with P-cadherin (blue) or E-cadherin (red). In e, n=26 beads pooled from 9 independent wells for siCT/Ecad beads; n=22 beads pooled from 9 independent wells for siVcl/Ecad beads; n=22 beads pooled from 9 independent wells for siCT/Pcad beads; n=23 beads pooled from 9 independent wells for siEcad/Pcad beads; n=36 beads pooled from 9 independent wells for siEcad/siVcl/Pcad beads. Data are represented as mean+SEM. * indicates $p<0.05$, *** indicates $p<0.001$ when compared with siCT. n.s. indicates non-significant comparisons (Mann-Whitney Rank Sum t-test). Scale bar, 10 μm (a,b,c).

Europe PMC Funders Author Manuscripts